Check for updates

Spherical means-based free-water volume fraction from diffusion MRI increases non-linearly with age in the white matter of the healthy human brain

Tomasz Pieciak [a],[*], Guillem París [a], Dani Beck [b],[c],[d], Ivan I. Maximov [c],[e], Antonio Tristán-Vega [a], Rodrigo de Luis-García [a], Lars T. Westlye [b],[c],[f], Santiago Aja-Fernández [a],[*]

[a] Laboratorio de Procesado de Imagen (LPI), ETSI Telecomunicación, Universidad de Valladolid, Valladolid, Spain
[b] Department of Psychology, University of Oslo, Oslo, Norway
[c] NORMENT, Division of Mental Health and Addiction, Oslo University Hospital & Institute of Clinical Medicine, University of Oslo, Oslo, Norway
[d] Department of Psychiatric Research, Diakonhjemmet Hospital, Oslo, Norway
[e] Department of Health and Functioning, Western Norway University of Applied Sciences, Bergen, Norway
[f] KG Jebsen Centre for Neurodevelopmental Disorders, University of Oslo, Oslo, Norway

ARTICLE INFO

ABSTRACT

The term free-water volume fraction (FWVF) refers to the signal fraction that could be found as the cerebrospinal fluid of the brain, which has been demonstrated as a sensitive measure that correlates with cognitive performance and various neuropathological processes. It can be quantified by properly fitting the isotropic component of the magnetic resonance (MR) signal in diffusion-sensitized sequences. Using $N = 287$ healthy subjects (178F/109M) aged 25-94, this study examines in detail the evolution of the FWVF obtained with the spherical means technique from multi-shell acquisitions in the human brain white matter across the adult lifespan, which has been previously reported to exhibit a positive trend when estimated from single-shell data using the bi-tensor signal representation. We found evidence of a noticeably non-linear gain after the sixth decade of life, with a region-specific variate and varying change rate of the spherical means-based multi-shell FWVF parameter with age, at the same time, a heteroskedastic pattern across the adult lifespan is suggested. On the other hand, the FW corrected diffusion tensor imaging (DTI) leads to a region-dependent flattened age-related evolution of the mean diffusivity (MD) and fractional anisotropy (FA), along with a considerable reduction in their variability, as compared to the studies conducted over the standard (single-component) DTI. This way, our study provides a new perspective on the trajectory-based assessment of the brain and explains the conceivable reason for the variations observed in FA and MD parameters across the lifespan with previous studies under the standard diffusion tensor imaging.

1. Introduction

Brain imaging has provided strong evidence that the human brain varies throughout the lifespan (Sowell, 2003; Westlye et al., 2010; Lebel et al., 2012; Bethlehem et al., 2022). A recent multiple-sites study by Bethlehem et al., (2022) reported that, during adulthood, there is a systematic reduction in gray matter and white matter (GM, WM) volumes, coupled with ventricles augmentation and an associated apparent thinning of the cerebral cortex. In addition, it has been found that differences in brain properties also exist between male and female brains,

accentuating with age (Sowell et al., 2007; Bethlehem et al., 2022). Accurate delineations of age-related trajectories of brain structural features can help us better understand its functioning and discern which patterns can be considered as "normative trajectories" (Bethlehem et al., 2022; Rutherford et al., 2022). Deviations from the regular patterns could be indicators of neurodevelopmental disorders as well as relevant markers for the diagnosis and prognosis of brain pathologies (Planche et al., 2022).

Age-related structural differences in the human brain were initially investigated in *post-mortem* cross-sectional studies (Dekaban et al.,

1978), which allowed to draw a plethora of conclusions on several features of the aging brain, such as reduced brain volume, enlarged ventricles and sulcal expansion (Skullerud, 1985; Kemper, 1994) and a general loss of neuronal bodies in the neocortex, hippocampus and cerebellum (Ellis, 1920; Nairn et al., 1989; Pakkenberg and Gundersen, 1997; Šimić et al., 1997). However, these studies were not exempt from some concerns regarding not only the (by default) nature of *post-mortem* studies but also of structural deviations from specimen treatment and volumetric changes during preservation (Skullerud, 1985; Allen et al., 2002). By addressing these issues, more recent research has observed brain variations *in vivo* with magnetic resonance imaging (MRI) (Sowell, 2003; Gogtay et al., 2004; Bethlehem et al., 2022). The diversity of MRI-derived modalities has enabled us to inspect the properties of various tissues and brain regions across the lifespan from both structural and microstructural perspectives (MacDonald and Pike, 2021). As previously stated, the WM is one of two major brain tissues, and it effectively alterates with age due to axonal shrinkage with the progressive oligodendrocyte death, demyelination with the formation of myelin spheroids and myelin debris accumulation during senescence (Peters 2002; Nave, 2010; Hill et al., 2018). The fluctuations in microstructural properties of the brain are associated with a range of physical and inherent biological processes, including cognition (Maillard et al., 2019), normal aging (Westlye et al., 2010; Lebel et al., 2012; Cox et al., 2016; Beck et al., 2021; Kiely et al., 2022) and the development of neurodegenerative diseases (Kubicki et al., 2007; Raghavan et al., 2021).

Diffusion magnetic resonance imaging (dMRI) has been widely applied to the study of healthy brain development and the aging (Bennett et al., 2010; Burzynska et al., 2010; Westlye et al., 2010; Lebel et al., 2012; Billiet et al., 2015; Chang et al., 2015; Cox et al., 2016; Kodiweera et al., 2016; Merluzzi et al., 2016; Beck et al., 2021), as well as neurological disorders that occur throughout life (Head et al., 2004; Cetin-Karayumak et al., 2020). dMRI allows the characterization of the diffusivity of water molecules within tissues, providing information about the microscopic configuration and structural connectivity of the brain. The most relevant feature of dMRI is its ability to measure the directional variance of water diffusivity in a single voxel, i.e. diffusion anisotropy (Basser et al., 1994). Different mathematical representations are used to describe the relationship between the acquired dMRI signal and the properties of the tissue under study. The most common way to estimate the diffusivity properties is *via* the single-component diffusion tensor imaging (DTI), representing the hindered diffusion that follows a Gaussian-like behavior (Basser et al., 1994; Westin et al., 2002; Assaf et al., 2004) and the derived scalars, such as the fractional anisotropy (FA) or the mean diffusivity (MD). These single-component DTI-based measures exhibit a well-documented curvilinear U-form across the lifespan in the healthy human brain, i.e. a rapid growth of FA parameter in early stages of life and a systematic decline after the peak value, consistent with the MD measure, which reveals the opposite trend (Westlye et al., 2010; Lebel et al., 2012; Beck et al., 2021).

Alternatively, there are other dMRI signal representations that can be used to quantify diffusion properties, with particular focus on the WM (Jensen et al., 2005; Özarslan et al., 2013; Tristán-Vega and Aja-Fernández, 2021). Despite their far-reaching abilities to represent Gaussian or non-Gaussian diffusion, the simplest extension of DTI is to assume that, inside the brain tissues, we can consider two different compartments, one related to the neural cells representing the hindered diffusion (the part that can be measured by the DTI) and another presenting the free-water diffusion that could be found as the cerebrospinal fluid (CSF), i.e., the diffusion that is neither restricted nor hindered (Pierpaoli and Jones, 2004; Pasternak et al., 2009; Hoy et al., 2014; Rydhög et al., 2017; Golub et al., 2021). An attractive characteristic of such a two-component representation is the free-water volume fraction (FWVF) parameter, which is defined as the fitted fraction of dMRI signal representation that could be attributed to isotropic diffusion with a fixed diffusivity of free water (e.g., $3.0 \cdot 10^{-3}$ mm^2/s is assumed for the *in vivo*

acquisitions) (Pasternak et al., 2009; Rydhög et al., 2017).

The FWVF can be estimated from dMRI data sets in a number of different ways. Biophysical models (Zhang et al., 2012; Cox et al., 2016; Raghavan et al., 2021) can imitate the underlying geometry of intra-voxel neural tissue, including the extracellular water diffusion, but the reproducibility and reliability of the FWVF parameter are relatively low (Chung et al., 2016; Lucignani et al., 2021). On the other hand, the bi-tensor scheme based on the aforementioned two-component representation (Pierpaoli and Jones, 2004; Pasternak et al., 2009) can resolve the FWVF and FW corrected DTI measures even from a standard single-shell dMRI acquisition (Pasternak et al., 2009; Golub et al., 2021), but the approach requires a carefully selected initialization of the fitting procedure. The multi-shell protocols with dedicated numerical optimization schemes are therefore preferred (Pasternak et al., 2012; Hoy et al., 2014; Bergmann et al., 2020), as the specificity of single-shell FW corrected DTI is not guaranteed (Golub et al., 2021). The bi-tensor approach, however, suffers from a positive bias observed in the voxels presenting complex architectures such as fiber crossings (Tristán-Vega et al., 2022), which are known to be present in up to 90% of the white matter voxels (Jeurissen et al., 2013). Alternatively, we will use the so-called spherical means technique (Kaden et al., 2016; Tristán-Vega and Aja-Fernández, 2021), in which the signals obtained for all orientations of the diffusion gradients with the same magnitude are averaged together. This way, the impact of a varying number of crossing fibers and confounding factors (i.e., the number of diffusion-sensitizing gradients) is removed, and the FWVF can be unbiasedly estimated over the WM whenever two different gradient magnitudes are included in the protocol (Tristán-Vega et al., 2022).

Several recent studies have shown that the variations in the single-shell FWVF may be related to cognitive performance (Maillard et al., 2019), or could be linked with neuroinflammation or atrophy of the aging brain (Metzler-Baddeley et al., 2012; Pasternak et al., 2012; Pasternak et al., 2016; Kubicki et al., 2019). Examples of conditions leading to increased single-shell FWVF values include parenchymal edema, such as those around tumors (Pasternak et al., 2009), Parkinson's disease (Ofori et al., 2015), first-episode of psychosis (Lyall et al., 2018), Alzheimer's disease (Bergamino et al., 2021) and schizophrenia (Carreira Figueiredo et al., 2022). The main implication of recovering FWVF information is related to the palliation of partial volume effects created by free-water diffusion (Metzler-Baddeley et al., 2012), given that DTI-based metrics are often contaminated with such, and its elimination results in the reduction in the number of false-positive streamlines in DTI-based tractography (Pasternak et al., 2009), an increased reproducibility (Albi et al., 2017) and sensitivity and specificity of the FW corrected diffusion tensor measures (Bergamino et al., 2016; Bergamino et al., 2021). The FW-corrected DTI has been found as a valuable tool in clinical scenarios including the predictions of glioblastoma recurrence in peritumoral edema (Metz et al., 2020) and neurological recovery of comatose patients after cardiac arrest (Keijzer et al., 2023), and the association of pedunculopontine nucleus degeneration with cognitive symptoms in Parkinson's disease (Ray et al., 2023). In addition, recent studies have suggested that the single-shell FWVF parameter is positively correlated with age in healthy humans' (Chad et al., 2018) and adult rhesus monkeys' (Kubicki et al., 2019) brains WM, and could therefore affect the evolution in DTI-related parameters across the lifespan (Metzler-Baddeley et al., 2012; Chad et al., 2018; Kubicki et al., 2019). All in all, however, it is not known how these single-shell FWVF variations with age generalize to the multi-shell FWVF as a detailed description of the evolution of multi-shell FWVF across the adult lifespan and its possible effects on diffusional properties of the brain WM have not been clarified.

This paper goes beyond the single-shell dMRI acquisitions and investigates how the FWVF estimated from multi-shell dMRI *via* the spherical means technique varies over the adult lifespan in the WM of the healthy human brain using cross-sectional and longitudinal data. The main contributions of this work are the following: we demonstrate

that (1) the FWVF varies non-linearly in the healthy human brain WM across the adult lifespan with a significant positive gain after the sixth decade of life; (2) the FWVF exhibits a heteroskedastic pattern with age; (3) we observe a region-specific dependence in the FWVF evolution, with the most pronounced shift in the cingulum (hippocampus; CGh), posterior thalamic radiation (PTR) and the genu of the corpus callosum (GCC) and (4) the presence of a spatial gradient of the water fraction. We observe that (5) the FWVF displays correlations with the brain, cerebral WM and ventricles volumes highlighting the heteroskedastic nature of the parameter as a function of the volume-based feature. Finally, (6) we have detected a huge influence of the FWVF on the variabilities of measures derived from DTI such as MD and FA across the adult lifespan. This variability can be significantly reduced when removing the bias modeled by the spherical means-based multi-shell FWVF.

2. Materials

2.1. Recruitment procedure, exclusion criteria and sample population

In total, $N = 287$ healthy subjects (178F/109M), aged (F/M mean $\pm$ std.dev: 60.6 $\pm$ 12.7/63.7 $\pm$ 15.0) were scanned after obtaining informed consent. Out of the 287 subjects, 99 were scanned again after periods between 10 and 30 months. Inclusion criteria for the study included being above the age of 18 years and absence of alcohol and drug dependence. The exclusion criteria included neurological and mental disorders, and suffering from a previous head trauma. Participants were also excluded if they were not compatible for MRI scanning, including being pregnant at the time of data collection or having pacemakers or metal implants. The participants completed comprehensive clinical and neuropsychological/cognitive assessments, blood sampling, and multimodal neuroimaging. The population was made up of largely ethnic Scandinavian and Northern European individuals. The demography across the age intervals including the full scale intelligence quotient (FSIQ) score and years of education are summarized in Table 1, while in Fig. 1, we visualize the population distribution of the study and time periods between two scans for 99 subjects.

2.2. MRI data acquisition

All subjects were scanned at Oslo University Hospital with a 3T General Electric Discovery MR750 scanner (GE, Waukesha, WI) equipped with a 32 channel head coil and a maximum gradient strength of 40 mT/m.

Diffusion MRI: The multi-shell diffusion MRI data were collected using an echo-planar imaging (EPI) sequence with the following parameters: time echo TE=83.1 ms, repetition time TR=8150 ms, flip angle 90°, voxel size 2 × 2 × 2 mm³, field-of-view FOV 256 × 256 mm², acquisition matrix 128 × 128 and 66 slices covering the

Table 1
Population distribution used in the study ($N = 287$ healthy cases, 178F/109M) including the FSIQ and years of education (mean $\pm$ std. dev).

Age interval	Females (%)	Males (%)	FSIQ	Education (years)
20 ≤ Age < 30	3 (1.7%)	5 (4.6%)	113.1 ± 7.2	14.9 ± 2.2
30 ≤ Age < 40	10 (5.6%)	6 (5.5%)	112.9 ± 9.6	16.9 ± 2.0
40 ≤ Age < 50	25 (14.0%)	8 (7.2%)	113.8 ± 11.2	17.0 ± 2.3
50 ≤ Age < 60	36 (20.2%)	15 (13.8%)	117.6 ± 9.9	16.4 ± 3.0
60 ≤ Age < 70	58 (32.6%)	27 (24.8%)	116.8 ± 12.8	15.3 ± 3.1
70 ≤ Age < 80	43 (24.2%)	44 (40.4%)	120.5 ± 12.9	16.0 ± 3.4
80 ≤ Age < 90	2 (1.1%)	3 (2.8%)	129.0 ± 12.6	20.6 ± 4.8
90 ≤ Age < 100	1 (0.6%)	1 (0.9%)	120.0 ± 4.0	16.0 ± 2.0

brain. The data were acquired under two b-shells at $b = 1000$ s/mm² and $b = 2000$ s/mm² along with non-collinear 60 and 30 uniformly distributed diffusion gradient directions per shell, respectively. Each session included ten non-diffusion-weighted volumes (i.e., $b = 0$) and additionally seven non-diffusion-weighted volumes acquired in a reversed phase-encoding direction used to correct the susceptibility distortions. Total scan time was 8 min 58 sec.

T1-weighted MRI: The structural T1-weighted data were collected using a 3D inversion recovery prepared fast spoiled gradient recalled sequence (IR-FSPGR; BRAVO) using the following parameters: TE=3.18 ms, TR=8.16 ms, flip angle 12°, voxel size 1 × 1 × 1 mm³, FOV 256 × 256 mm², acquisition matrix 128 × 128 and 66 slices covering the brain. Total scan time was 4 min 43 sec.

The initial population sample underwent a QA protocol, including testing for head motions, noise, and other acquisition-related artifacts. Additionally, the data sets were manually inspected if the temporal signal-to-noise-ratio parameter (Roalf et al., 2016) deviated ±2.5 standard deviation from the mean value.

2.3. Data preprocessing

Diffusion MRI: The data were preprocessed using the pipeline adapted from Maximov et al. (2019), including noise removal using the Marčenko-Pastur principal component analysis technique (Veraart et al., 2016; https://github.com/NYU-DiffusionMRI/mppca_denoise), Gibbs ringing artifacts correction (Kellner et al., 2016; https://bitbucket.org/reisert/unring), susceptibility-induced distortions (Andersson et al., 2003) using the FSL FMRIB Software Library v6.0.1 `topup` tool (Analysis Group, FMRIB, Oxford, UK.; Smith et al., 2004; https://fsl.fmrib.ox.ac.uk/fsl/fslwiki), head movements and eddy current distortions correction using the FSL `eddy` tool.

T1-weighted MRI: The data were processed using the FreeSurfer 5.3 image analysis suite (http://surfer.nmr.mgh.harvard.edu; `recon-all` command), including non-uniformity intensity correction, computation the Talairach transform, skull stripping and the non-linear volumetric registration. The brain labeling was performed using the automatic subcortical segmentation using the probabilistic atlas (Fischl et al., 2002). The following volume-based features are considered in the study: total intracranial volume (TIV), brain volume, brain volume without ventricles and cerebral WM volume.

3. Methods

This section presents the methodologies used to estimate the FWVF and DTI-based parameters under the standard DTI and FW compensated DTI, the data registration procedure and the statistical tools used to model the changes in the studied brain parameters. For a single subject, we calculated: (1) the volume-based features of the brain from T1-weighted scans, (2) the FWVF parameter f from two-shell dMRI data acquired at $b = \{1000, 2000\}$ s/mm² using the spherical means approach (Tristán-Vega et al., 2022), (3) the standard DTI-based MD and FA measures from single-shell dMRI data at $b = 1000$ s/mm² and (4) the FW corrected equivalent DTI-based measures from single-shell dMRI data at $b = 1000$ s/mm² given the estimated FWVF f in the two-component representation. Twenty three regions of interest (ROIs) from the Johns Hopkins University (JHU) WM atlas (Mori et al., 2005) are used in the study in order to evaluate the region-specific properties of FWVF and DTI-based measures of the brain.

3.1. Free-water volume fraction (FWVF) estimation

The FWVF parameter f was estimated from a two-shell diffusion MRI acquisition using the spherical means approach (Tristán-Vega et al., 2022) that assumes the diffusion is modeled using a continuous mixture of axis-symmetric second-order tensors in the space of orientations. The
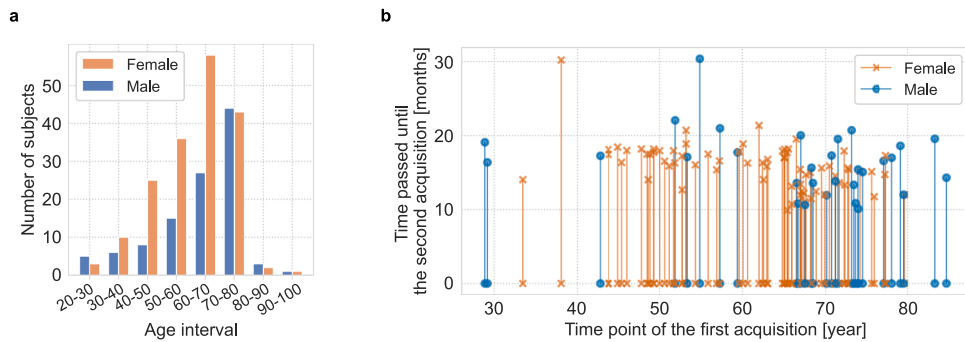
Figure 1. a The demography of the study ($N = 287$ healthy cases, 178F/109M) ordered into the age intervals. A single group includes all subjects at age greater or equal to the left range and lower to the right range. b Graph presenting the first acquisition time point (in years; horizontal axis) and the time passed until the second acquisition (in months; vertical axis). The second acquisition is available for 99 out of 287 subjects.

normalized dMRI signal is represented as follows (Tristán-Vega and Aja-Fernández, 2021; Tristán-Vega et al., 2022):

$$\frac{S(\boldsymbol{g},b)}{S(0)} = (1-f)\int\int_\Omega \Phi(\boldsymbol{v})\exp\left(-b(\lambda_{\text{par}}-\lambda_{\text{per}})\left(\boldsymbol{v}^T\boldsymbol{g}\right)^2 - b\lambda_{\text{per}}\right)d\boldsymbol{v} + f\exp(-bD_0),$$

(1)

where $f \in [0, 1]$ is the FWVF parameter, $\boldsymbol{g}$ is the diffusion sensitizing gradient direction, b is the b-value, $\Phi(\boldsymbol{v}) \geq 0$ is the convolution kernel, $\Omega = \{\boldsymbol{v} \in \mathbb{R}^3 : ||\boldsymbol{v}|| = 1\}$, λ_{par} and λ_{per} are the longitudinal and perpendicular diffusivities that satisfy the formula $0 \leq \lambda_{\text{per}} \leq \lambda_{\text{par}} \leq D_0$ with $D_0 = 3.0 \cdot 10^{-3}$ mm^2/s being the apparent diffusion coefficient of free-water given for a water temperature of 37°C (Pasternak et al., 2009). The FWVF f from Eq. (1) was found by optimizing the following cost function:

$$\{\widehat{f}, \widehat{\lambda_{\text{per}}}\} = \text{argmin}_{f,\lambda_{\text{per}}} \frac{1}{2}\sum_{j=1}^{M}\left(\log\left(\frac{\overline{s}_j - (1-f)\exp(-b_jD_0)}{f}\right) + b_j\lambda_{\text{per}}\right.$$

$$\left. + \log\left(\frac{2\sqrt{b_j(\lambda_{\text{par}}-\lambda_{\text{per}})}}{\sqrt{\pi}\text{erf}\left(\sqrt{b_j(\lambda_{\text{par}}-\lambda_{\text{per}})}\right)}\right)\right)^2 + \nu\frac{\lambda_{\text{per}}}{\lambda_{\text{par}}-\lambda_{\text{per}}}$$

(2)

with $\overline{s}_j$ being the orientationally-averaged dMRI signal for j-th shell ($j = 1, ..., M$) via the spherical harmonics decomposition at the order of $L = 6$ using an inverse linear problem with a Laplace-Beltrami regularization at $\lambda = 0.001$, b_j is j-th b-value ($b \in \{1000, 2000\}$ s/mm^2) and $\nu = 0.06$ is the penalty term that promotes the prolate convolution kernels. The Eq. (2) was solved using a constrained optimization via the gradient-projection method by fixing the parallel diffusion $\lambda_{\text{par}} = 2.1 \cdot 10^{-3}$ mm^2/s. The FWVF was estimated with the dMRI-Lab toolbox (https://www.lpi.tel.uva.es/dmrilab) implemented in MATLAB (The MathWorks, Inc., Natick, MA).

3.2. Diffusion tensor imaging (DTI) under a two-component representation

The DTI-based metrics were estimated under two variants, namely a standard approach proposed by Basser et al. (1994) and a two-component representation illustrating the hindered diffusion via a diffusion tensor and free diffusion by a mono-exponential decay (Pierpaoli and Jones, 2004; Pasternak et al., 2009):

$$\frac{S(\boldsymbol{g},b)}{S(0)} = (1-\widehat{f})\exp(-b\boldsymbol{g}^T\boldsymbol{D}\boldsymbol{g}) + \widehat{f}\exp(-bD_0), \quad \widehat{f} \in [0, 1]$$

(3)

with $\widehat{f}$ being the pre-estimated FWVF parameter using the spherical means approach (Tristán-Vega et al., 2022), and $\boldsymbol{D}$ is a symmetric semi-positive matrix of size 3×3 representing the hindered diffusion.

The two-component representation given by Eq. (3) reduces to the standard DTI for $\widehat{f} = 0$.

To estimate the diffusion tensor $\boldsymbol{D}$ in either representation, we used the least squares approach solving the system of linear equations $\boldsymbol{d} = (\boldsymbol{X}^T\boldsymbol{X})^{-1}\boldsymbol{X}^T\log(\boldsymbol{S})$ with $\boldsymbol{S}$ being the vector of dMRI signals acquired at $b = 1000$ s/mm^2, i.e., $\boldsymbol{S} = \frac{1}{1-\widehat{f}}\left[\frac{S(\boldsymbol{g_1},b)}{S(0)} - \widehat{f}\exp(-bD_0), ..., \frac{S(\boldsymbol{g_n},b)}{S(0)} - \widehat{f}\exp(-bD_0)\right]^T$, $\boldsymbol{d} = [D_{\text{xx}}, D_{\text{xy}}, D_{\text{xz}}, D_{\text{yy}}, D_{\text{yz}}, D_{\text{zz}}]^T$ is a vector representation of the diffusion tensor $\boldsymbol{D}$ and $\boldsymbol{X}$ is the encoding gradient design matrix. Two measures were obtained from either representation, namely the MD and FA. The DTI-based parameters were estimated with home-delivered software written in Python 3.8.5 (https://www.python.org) and NumPy 1.19.2 library (https://numpy.org).

3.3. Data registration and regions of interest retrieval

The FA parameters estimated using the standard DTI at $b = 1000$ s/mm^2 were used to register the data to the standard space and retrieve the JHU WM atlas labels in the native subjects' spaces (Mori et al., 2005). First, the FA parameters were affinely registered to the FSL template FMRIB58_FA via the FSL flirt tool (Analysis Group, FMRIB, Oxford, UK) using the normalized correlation cost function and a trilinear interpolation. We applied then a non-linear transformation (fnirt) and obtained a reverse warping to the subjects' native spaces via the FSL invwarp. The JHU WM regions of interest (Mori et al., 2005) were transformed to the subjects' native spaces using a nearest-neighbor interpolation. In order to eliminate potential misregistration outliers due to a partial volume effect the regions of interest were shrunk with a morphological binary erosion operator with a cubic kernel of size $2 \times 2 \times 2$.

3.4. Statistical analyses

The region-specific age-related trajectories in the FWVF f and DTI-based parameters across the adult lifespan are modeled using the quantile regression (QR) technique (Koenker and Hallock, 2001). Contrary to a standard polynomial regression the QR estimates the conditional median of the parameter and allows for modeling its heteroskedastic nature without any theoretical assumptions on the distributional properties of the data. Employing the QR technique, we can simultaneously model the non-linear behavior of the parameter with age and handle the variations in the parameter's fluctuations with age by considering different quantiles, e.g., the 5th and 95th percentiles.

Modeling the age-related trajectories of the FWVF f, MD and FA:

To model the variations in the parameter (i.e. f, MD, FA) given the explanatory variable *Age* being the subject's age at the scan time, and optionally to handle the continuous variable *FSIQ* or the binary variable *Sex*, we used the following models:

Model 1 $:Q(\tau|Age) = \beta_0 + \beta_1 Age + \beta_2 Age^2,$ (4)

Model 2 $:Q(\tau|Age, FSIQ) = \beta_0 + \beta_1 Age$
$+\beta_2 Age^2 + \beta_3 FSIQ + \beta_4 FSIQ \times Age,$ (5)

Model 3 $:Q(\tau|Age, Sex) = \beta_0 + \beta_1 Age$
$+\beta_2 Age^2 + \beta_3 Sex + \beta_4 Sex \times Age$ (6)

with $\beta_k \in \mathbb{R}$ being the unknown parameters to be estimated. The models given by Eqs. (5) and (6) enable us to additionally include two-way interactions between the variables *Age* and *FSIQ/Sex*. The optimal order of the polynomial as a function of the variable *Age* (i.e., the first-order or the second-order) for each ROI was selected using the Akaike information criterion (AIC) Akaike, 1974). The longitudinal observations from our sample population have been handled as independent in Eqs. (4)-(6).

Modeling the FWVF *f* as a function of volume-based features:

The first-order model is employed to model the FWVF parameter *f* as a function of volume-based features:

Model 4 $:Q(\tau|Feature) = \beta_0 + \beta_1 Feature,$ (7)

where *Feature* is the explanatory variable, i.e., the brain volume, cerebral WM volume or ventricles volume.

Model optimization in the QR framework:

The parameters $\boldsymbol{\beta} = [\beta_0, ..., \beta_{k-1}]$ in Eqs. (4-7) were found using the following formula:

$$\widehat{\boldsymbol{\beta}} = \mathrm{argmin}_{\boldsymbol{\beta}\in\mathbb{R}^k} \sum_{i=1}^{N} \rho_\tau\left(y_i - \boldsymbol{x}_i^T\boldsymbol{\beta}\right) \mathrm{with}\, \rho_\tau(r) = r\cdot\left(\tau - I_{(-\infty,0)}(r)\right), \quad (8)$$

where $x_i = [1,\ Age_i,\ ...]$ is the *k*-th dimensional vector of covariates, y_i is the response variable from *i*-th subject of the study (i.e., the median value over the ROI) and $I_{(-\infty,\ 0)}(r)$ is the indicator function. The Eq. (8) is optimized using Brent's method (Brent, 1973). For all models, we calculated the quantile function $Q(\tau|Age)$ under three quantiles τ, i.e., $\tau = 0.05$ (5th percentile), $\tau = 0.5$ (median), and $\tau = 0.95$ (95th percentile).

Goodness-of-fit in QR: To calculate the goodness-of-fit of the model fitted with the QR framework under the quantile τ, we used the coefficient R^1 introduced by Koenker and Machado (1999):

$$R^1(\tau) = 1 - \frac{V_k(\tau)}{V_1(\tau)} \text{ with } V_k(\tau) = \min_{\boldsymbol{\beta}\in\mathbb{R}^k} \sum_{i=1}^{N} \rho_\tau\left(y_i - \boldsymbol{x}_i^T\boldsymbol{\beta}\right), \quad (9)$$

where $V_1(\tau)$ and $V_k(\tau)$ are the parameters calculated with the non-conditional model (i.e., intercept only) and the conditional model, respectively.

Doane's formula: The number of bins N_h used to compute a single density plot given the sample of size *h* was calculated upon Doane's formula (Doane, 1976):

$$N_h = \left\lfloor \gamma\cdot(1 + \log_2(h) + \log_2\left(1 + \frac{\sqrt{\widetilde{\mu}_1}}{\sigma_1}\right)\right\rfloor \quad (10)$$

with the statistics $\sqrt{\widetilde{\mu}_1}$ being the third standardized sample moment and $\sigma_1 = \sqrt{\frac{6(h-2)}{(h+1)(h+3)}}$ being the standard deviation of $\sqrt{\widetilde{\mu}_1}$. The scalar $\gamma > 0$ is the scaling factor and $\lfloor y \rfloor$ is the function that provides the largest integer number less than or equal to *y*.

Breusch-Pagan (BP) test: The BP statistical test was used to assess the heteroskedasticity in the FWVF *f* as a function of volume-based parameters. The null hypothesis H_0 of the test states that the error variances of the linear model are equal (i.e., the homoskedasticity present in the FWVF *f*), while the alternative hypothesis H_1 states that the error variances are not equal, i.e., heteroskedasticity exists in the FWVF parameter (Breusch and Pagan, 1979). We used the studentizing

correction to the BP test as suggested by Koenker (1981).

Software: All statistical analyses were carried out with GNU R 4.1.2 using the quantreg, DescTools and lmtest (https://cran.r-project.org/web/packages) packages and Statsmodels library 0.12.0 (https://www.statsmodels.org) handled with Python 3.8.5.

4. Experiments and results

4.1. Free-water volume fraction shows a non-linear trend with age

In this first section, we study the region-specific changes in the spherical means-based FWVF estimated from multi-shell dMRI across adulthood and evaluate the possible effects from sex and intelligence variables. For the sake of illustration, a preliminary visual inspection of the FWVF parameter is performed for three different slices and for eight different age intervals across the adult lifespan (see Fig. 2a). Each map shows voxel-wise median aggregated water fractions in the common space from all subjects available in a specified range (see Table 1). We observe a non-uniform FWVF with higher values in the anterior part of the brain compared to the medial regions. These variations are especially pronounced beginning from the interval $60 \le Age < 70$ (Fig. 2a, first row). Furthermore, we observe heightened FWVFs in the regions close to the CSF, highlighted with succeeding age intervals.

In Fig. 2c we illustrate the trajectories of the FWVF *f* over the whole WM area and eight selected regions of interest (ROIs) across the adult lifespan (see Supplementary Fig. 1 for the remaining 14 ROIs). Each marker relates to a single subject and displays a median value of *f* calculated from all samples available per ROI. The trajectories are modeled with the QR technique (Koenker and Hallock, 2001) *via* a polynomial of the variable *Age* (Model 1). We present the quantile function $Q(\tau|Age)$ under three quantiles, i.e. $\tau = \{0.05,\ 0.5,\ 0.95\}$. Further details, including the coefficients of the models for the different ROIs, their standard errors and *p*-values, are gathered in Supplementary Table 1.

In the whole WM area, we observe a non-linear behavior of the FWVF *f* across the adult lifespan that follows the model obtained at $\tau = 0.5$ (50th percentile) given by the equation:

$$Q(0.5|Age) = 0.197052 - 0.260578 \times 10^{-2}\cdot Age + 0.27289 \times 10^{-4}\cdot Age^2$$

with $p < .001$ for all coefficients and the goodness-of-fit equals $R^1 = 0.107$. The standard errors for the coefficients are 0.22176×10^{-1} (β_0), 0.70786×10^{-3} (β_1) and 0.6351×10^{-5} (β_2); note all three are one order of magnitude smaller than the corresponding coefficients. The age peak indicates the trend reversal in the FWVF over the WM at the age of 47y 9m. Regarding individual ROIs, we generally recognize a positive non-linear U-shaped trend represented by the second-order polynomial within most WM regions except for the cingulum (cingulate gyrus; CGg), cerebral peduncle (CP), superior cerebellar peduncle (SCP) and medial lemniscus (ML) where the first-order model slightly better represents the FWVF behavior in terms of the AIC (Akaike, 1974). The significance of the quadratic term in the second-order models varies across the regions within the range $p < .001$ and $p < .05$ excluding two regions, namely the PTR ($p = .055$) and inferior cerebellar peduncle (ICP; $p = .099$). The trend reversal also varies in a region-specific manner spreading from 27y 10m (PTR) to 56y 8m corticospinal tract (CT). Importantly, the QR technique allows for covering different quantiles over the data. We observe that the quantile functions $Q(0.05|Age)$ and $Q(0.95|Age)$ increase the distance between each other with age for most regions considered in the study. These results suggest that the median FWVF *f* exhibits a heteroskedastic nature, i.e., the parameter variability increases with age.

In order to evaluate the possible effects from sex and intelligence over the results, we extended the analysis and incorporated (1) the *FSIQ* variable (Model 2) and (2) the binary variable *Sex* (Model 3), and verified the two-way interactions between the variables for both models,
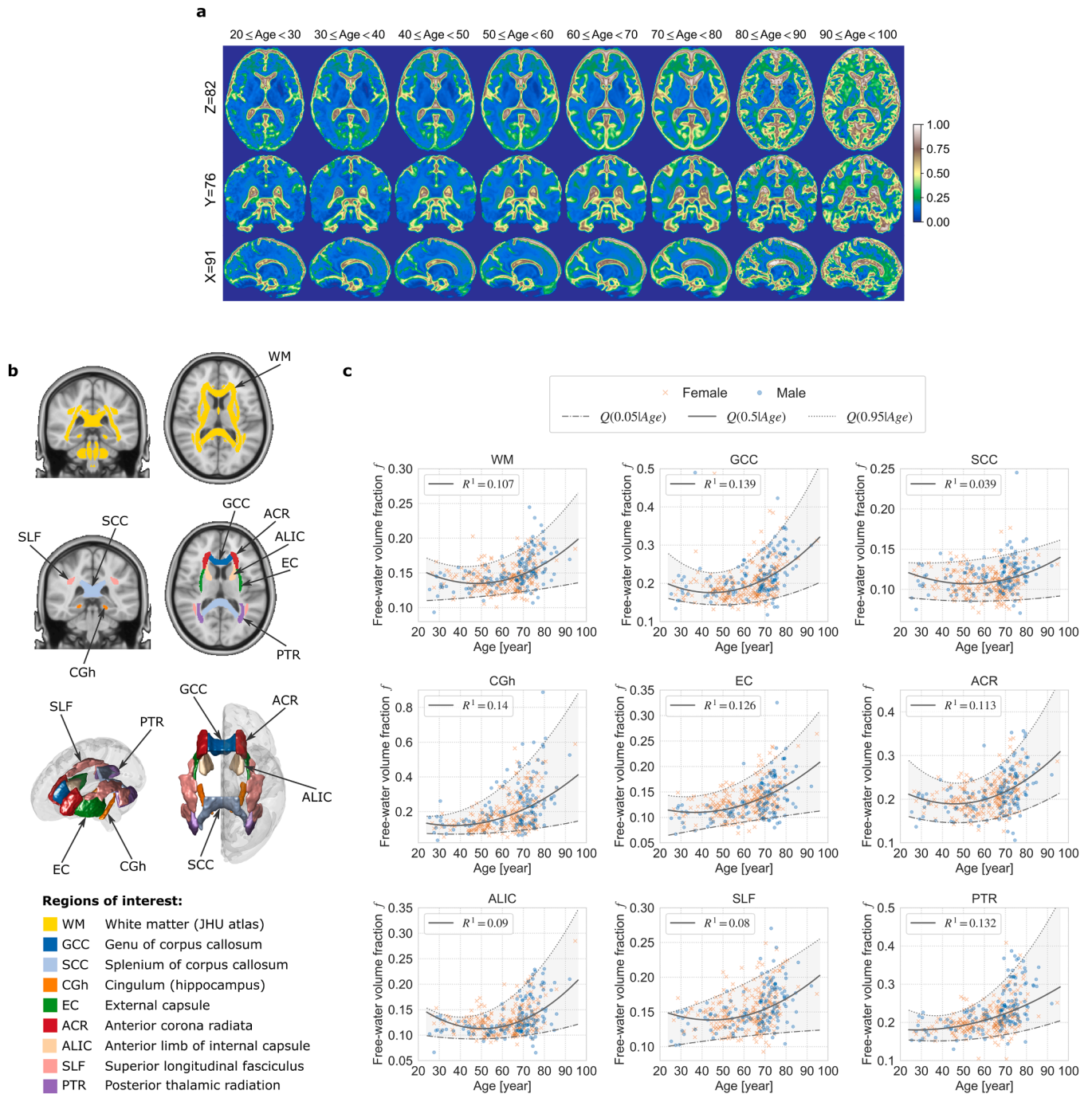
Figure 2. The trajectories of the FWVF parameter across the study age span shown over different regions of interest (ROIs). a Visual inspection of the FWVF f across age intervals presented separately in axial (Z=82), coronal (Y=76) and sagittal (X=91) planes. The images are displayed in the standard space after non-linear warpings computed with the single-component FA registration from the subjects' native spaces. Each figure presents a median image of the FWVF f computed voxel-wise across all subjects available in a specified range (only cross-sectional samples are used for this experiment). b The ROIs used in the study were retrieved from the JHU DTI-based atlas (Mori et al., 2005) and visualized in the standard space over the T1-weighted coronal and axial slices, and using 3D models. c Estimated FWVFs and their trajectories computed with a quantile regression technique using Model 1 (see Eq. (4) in Methods). An individual marker delivers a median value of the FWVF f computed from the ROI in the native space of a single subject. The experiment uses cross-sectional and longitudinal samples. The quantile function $Q(\tau|Age)$ for a single ROI is shown under three quantiles, i.e., the solid line presents $Q(\tau|Age)$ under $\tau = 0.5$ (50th percentile), the lower thin dashed-dotted line indicates $Q(\tau|Age)$ under $\tau = 0.05$ (5th percentile), and the upper thin dotted line presents $Q(\tau|Age)$ under $\tau = 0.95$ (95th percentile). All three were computed from median FWVFs. The regions between $Q(0.05|Age)$ and $Q(0.95|Age)$ were shaded for visualization purposes. The goodness-of-fit R^1 at $\tau = 0.5$ was computed for each region using the procedure introduced by Koenker and Machado (1999).

i.e. *FSIQ × Age* and *Sex × Age*. The results show no main effects from the *FSIQ* and no interactions *FSIQ × Age* over all ROIs considered in the study at the significance level of 0.05 (see Supplementary Table 2). Regarding the gender, we recognize that the variable *Sex* is statistically significant at the level of 0.05 in four regions, namely the sagittal stratum (SS; $p < .01$), and SCP, CT, ML, all three at $p < .05$, and significant interaction term *Sex × Age* over five ROIs, i.e. WM, PTR, SCP and ML ($p < .05$) and SS ($p < .001$) (see Supplementary Table 3).

4.2. Free-water volume fraction exhibits heteroskedastic region-specific variations with age

The experiments included in this section illustrate the variability of the FWVF across the adult lifespan and uncover these variations quantitatively. First, in Fig. 3a, we present the region-specific population density plots of the FWVF over the age intervals for the whole WM and seven selected ROIs (see more ROIs in Supplementary Fig. 2). Each density plot aggregates the water fraction values directly from the subjects' native spaces. Since different regions of the brain are characterized by different sizes and the age intervals are not evenly split in our population sample, the numbers of bins are defined dynamically, being proportional to Doane's formula (see Eq. (10)). The experiment reveals that (1) the population density plots are bell shaped (positively skewed) through all age intervals and (2) the density plots increase the tails and the mode of the density plots shifts positively along successive age decades.

Next, in Fig. 3b, we report the population FWVF values for the whole WM and the GCC using box plot representation, median values, and interquartile ranges (IQRs) for each age interval (the box plots for remaining ROIs can be found in Supplementary Fig. 3). The experiment reveals that the population median FWVF varies over the WM between 0.13 for base age interval $20 \leq Age < 30$ and 0.16 under $80 \leq Age < 90$, and it begins to accelerate after the sixth decade of life. Note that this variation increases for other ROIs, like GCC, where it ranges from 0.18 to 0.27. Essentially, the FWVF is a region-specific parameter spanning from 0.09 for the middle cerebellar peduncle (MCP) to 0.19 for the anterior corona radiata (ACR) region, all reported for the base age interval. Importantly, we observe an increase in the dispersion of the water parameter represented by the IQR measure with age. The regions with a small median initial water fraction, e.g., MCP, ML, splenium of corpus callosum (SCC) and CP do not substantially increase their values across the age decades. In contrast, the areas characterized by higher median water fraction values such as the ACR, PTR, GCC, SS or posterior corona radiata (PCR) generally show the most substantial parameter growth under the ninth decade of life. In addition, note that these results suggest that the FWVF f exhibits a heteroskedastic nature, i.e., the parameter variability increases with age, as indicated by the general growth of the IQR in most regions (see Fig. 3b and Supplementary Fig. 3b,c).

Fig. 3c derives from this experiment and demonstrates the relative errors (given in %) of the median FWVF calculated between the successive intervals and the base interval $20 \leq Age < 30$. On average, the WM region is denoted by a relatively small increase in the FWVF until the sixth decade of life, and then it starts enhancing significantly, reaching the value of 16% in the ninth decade of life. The highest increase in the water fraction across the life decades has been observed for the CGh (+139.3%), PTR (+57.5%) and the GCC (+55.5%). Contrarily, we denote irregular alterations in the MCP, posterior limb of internal capsule (PLIC), CGg and CT regions with a tendency toward negative values in PLIC, CGg and CT measured at the age interval $80 \leq Age < 90$. This experiment also reveals an anterior-posterior spatial gradient of the FWVF, as recently suggested by Chad et al., (2018). More precisely, we observe the higher change rates in the GCC over SCC and anterior limb of internal capsule (ALIC) over PLIC (see the color frames included in Fig. 3c).

4.3. Free-water volume fraction correlates with volumetry-based features of the brain

In the next experiment, we correlate the FWVF f estimated from multi-shell dMRI with volumetry-based features, including brain, cerebral WM and ventricles volumes. Prior to that, however, we inspect the variations in the volumetric features for our database and their trajectories as a function of age, to ensure that the behavior matches that previously reported by other authors. Fig. 4a-c presents the variations in these features modeled using the second-order polynomial over the

relative values normalized by the TIV (see Supplementary Fig. 5 for the unnormalized plots). In general, we observe the U-shaped characteristics of the whole brain and cerebral WM volumes. The ventricles volume follows a systematic non-linear increase, also accentuating higher values in male subjects. The results obtained with this sanity test are consistent with previous literature reports (Lebel et al., 2012; Bethlehem et al., 2022).

Before studying the correlation between FWVF f and the volume-based features, we applied the studentized Breusch-Pagan (BP) test (Breusch and Pagan, 1979; Koenker, 1981) to verify the heteroskedasticity in the FWVF parameter as a function of the anatomical feature. The BP test results were as follows (see Supplementary Table 4):

1. FWVF f versus brain volume (females $\chi^2(1, N = 178) = 10.83$, $p < .001$, males $\chi^2(1, N = 109) = 6.47$, $p = .011$);
2. FWVF f versus cerebral WM volume (females $\chi^2(1, N = 178) = 5.02$, $p = .025$, males $\chi^2(1, N = 109) = 6.30$, $p = .012$); and
3. FWVF f versus ventricles volume (females $\chi^2(1, N = 178) = 3.37$, $p = .066$, males $\chi^2(1, N = 109) = 24.74$, $p < .001$).

These results suggest a heteroskedastic nature of the FWVF parameter as a function of the above-mentioned volume-based features in most cases under the significance level of 0.05. Therefore, the employment of the QR over a standard regression is well founded.

In Fig. 4d-e, we thus relate the FWVF medians calculated over the WM with three volumetry-based features and complement them with the first-order QR models. First, we notice that the linear coefficients for the volumes of the brain and ventricles at $\tau = 0.5$ are statistically significant under the significance level of 0.05 (see Supplementary Table 4). In contrast, the linear coefficient for the cerebral WM volume in females is not statistically significant under the level of 0.05 ($p = .133$), while in males, it approaches the borderline of significance ($p = .051$). For most statistically significant coefficients, we recognize the standard error as at least one order of magnitude smaller than the corresponding coefficient. The results show negative correlations of the FWVF parameter with brain volume (females $r = -0.266$, males $r = -0.439$) and cerebral WM volume (females $r = -0.220$, males $r = -0.335$), while there is a positive correlation between the FWVF and the ventricles volume (females $r = 0.415$, males $r = 0.497$), all under the significance of 0.01. Besides, the experiment reveals stronger correlations for males than for females in all three cases. Apart from the previously confirmed more notable variability of the FWVF with age (see Fig. 2c), here we identify more variable volumes with age that are coupled with higher FWVF values.

4.4. Correcting the DTI representation for the free-water volume fraction leads to flattening trajectories of mean diffusivity and fractional anisotropy measures across the adult lifespan

In this final section, we study the effect of the spherical means-based FWVF estimated from multi-shell dMRI on the DTI metrics estimated from single-shell dMRI across the adult lifespan. To that end, we explore the lifespan trajectories of MD and FA measures estimated from the two-component representation given by Eq. (3) and relate them to the standard DTI equivalents, where no FW is assumed. The variations in MD and FA are modeled again using the QR approach presenting now the conditional median of a DTI parameter given the explanatory variable *Age* (Model 1). For the sake of illustration, in Fig. 5a we visually demonstrate the variations of MD and FA parameters for a randomly chosen male subject at the age of 69. We observe considerable decreased (increased) values of the MD (FA) parameters in the FW compensated DTI scenario. The contours of the WM area become detectable with the FW corrected MD, while the FW compensation generally strengthens the FA measure. In Fig. 5b, we show the population density plots of MD and FA measures for WM, GCC and SCC, calculated from standard and FW
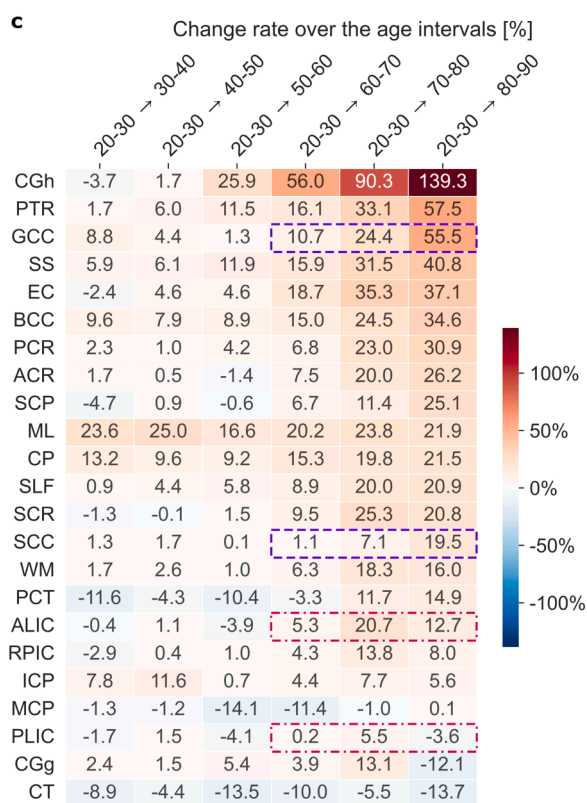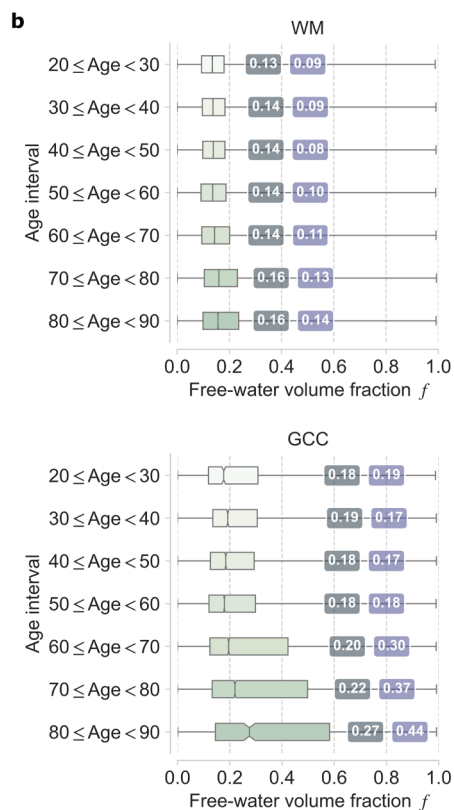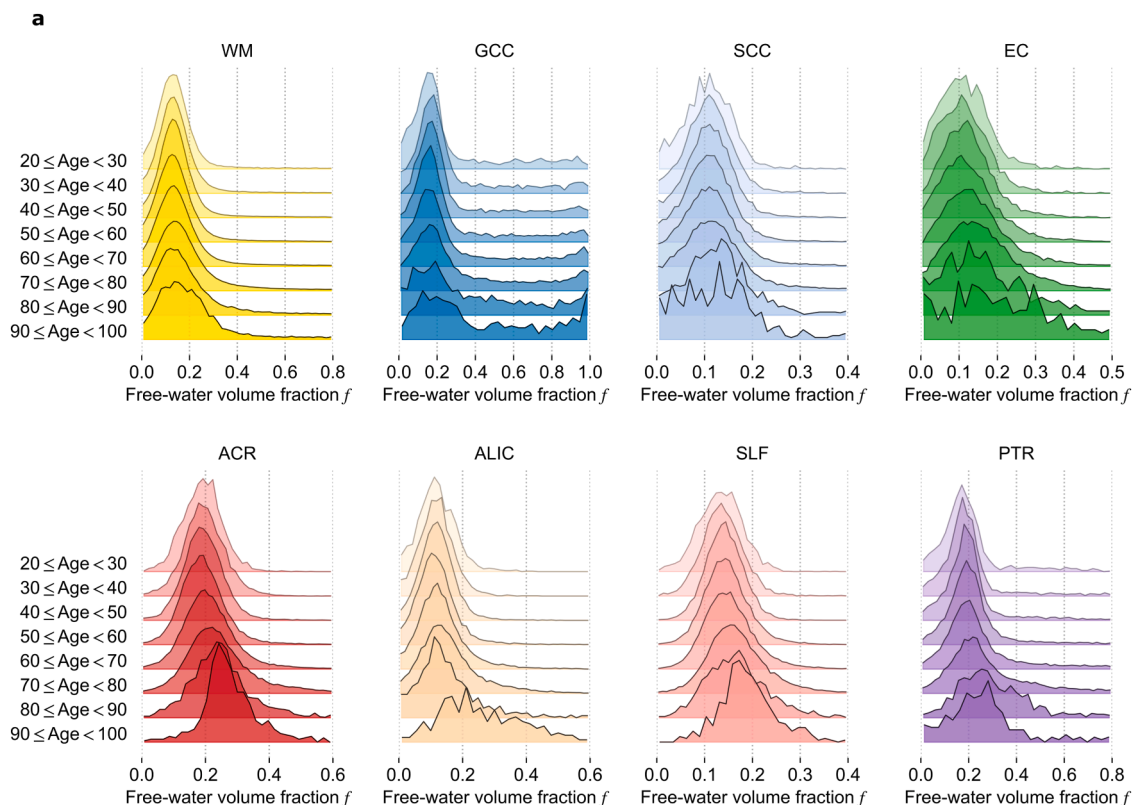
(caption on next page)

Figure 3. a The deviations in the population density plots of FWVF *f* presented over the age intervals defined in Table 1 and the eight WM ROIs from Fig. 2b. A single region is represented by eight normalized density plots, each constructed from all subjects' FWVFs per interval. Doane's method (Doane, 1976) was applied separately to each ROI and age interval to determine the optimal number of bins used to construct the density plot. The colors of the density plots follow those defined in Fig. 2b. b The quantitative fluctuations in the FWVF *f* over the WM and GCC and age intervals considered in the study. The box plots present the first, the second (median) and the third quartile, respectively. The whiskers denote minimal and maximal values of the FWVF over the ROIs, while the values over the box plots indicate the population median (first value) and the interquartile range, both calculated from all subjects available per age interval. We have not considered the age interval 90 ≤ *Age* < 100 in this population experiment owing to the presence of only two subjects aged over 90 in the cross-sectional sample. c The change rates in the FWVFs over the age intervals are summarized over all ROIs considered in the study. A single number refers to the relative change (in %) of the median FWVF, calculated for a given age interval, with respect to the median FWVF, obtained for the age interval 20 ≤ *Age* < 30. All FWVF's medians were obtained directly from the subjects' native spaces. The regions were sorted in descending order according to the values within the interval 80 ≤ *Age* < 90. The regions covered by the same frame colors follow the anterior-posterior spatial gradient (i.e., GCC-SCC and ALIC-PLIC). All population-based experiments report the FWVF variations using only cross-sectional samples.

compensated DTI representations, depicted over the age intervals previously defined (see more ROIs in Supplementary Fig. 6). The standard MD and FA parameters are typically more dispersed regardless of the age interval, with a positive (negative) shift of the peaks observed for the MD (FA) measure in elderlies.

Next, in Fig. 5c we represent the MD and FA indices as a function of age for the whole WM and three selected regions, all illustrated with and without the FW compensation (see more ROIs in Supplementary Fig. 7). The coefficients of the models fitted under both variants can be found in Supplementary Table 5 and Supplementary Table 6. In general, we observe a non-linear behavior of the standard DTI-based MD parameter over the WM ($p < .001$ for all model coefficients, $R^1 = 0.129$) with an increasing trend starting from the middle adulthood, and opposite to that for the FA parameter ($p < .05$ for the quadratic model coefficient, $R^1 = 0.072$), both consistent with previous reports (Westlye et al., 2010; Lebel et al., 2012; Beck et al., 2021). Once the FW correction is applied to the standard DTI, we recognize smaller (larger) values of FW compensated MD (FA) over the WM compared to standard DTI, i.e., $p < .001$ for all model coefficients and $R^1 = 0.096$ for the MD, and non-significant linear ($p = .136$) and quadratic ($p = .114$) model coefficients and $R^1 = 0.012$ for the FA measure. Besides, the heteroskedastic pattern of the FW corrected DTI measures with age is significantly reduced.

5. Discussion

The free-water fraction has become a relevant measure in neuroimaging, especially for modeling various types of brain damage (Ofori et al., 2015; Bergamino et al., 2021; Carreira Figueiredo et al., 2022). With its possible importance in age-related pathologies and aging processes (Chad et al., 2018; Edde et al., 2020, Berger et al. 2022), the evolution of this parameter across the adult lifespan has not been studied in detail. Most works that evaluate the microstructural changes in the brain with age based on diffusion MRI simply use a single-component DTI approach, where the FWVF is not taken into account (Burzynska et al., 2010; Bennett et al., 2010; Westlye et al., 2010; Lebel et al., 2012; Cox et al., 2016; Beck et al., 2021). The present study investigates precisely how the FWVF estimated from multi-shell dMRI varies across the adult lifespan in the healthy human brain WM, as well as its interference with DTI-based metrics. To that end, we employ the spherical means technique (Tristán-Vega et al., 2022) that robustly estimates the water fraction for complex neural architectures, such as fiber crossings, and a two-component dMRI signal representation to retrieve the FW compensated DTI measures.

Although previous studies have already determined that the single-shell bi-tensor FWVF and multi-shell biophysical-based FWVF are associated with age (Metzler-Baddeley et al., 2012; Billiet et al., 2015; Cox et al., 2016; Chad et al., 2018; Kubicki et al., 2019), in this study, we uncovered a positive trend with age and revealed a non-linear gain in the spherical means-based multi-shell FWVF parameter after the sixth decade of life over most WM areas (Fig. 2c, Supplementary Fig. 1b,d, Fig. 3b, Supplementary Fig. 3b). Our findings suggest a heteroskedastic nature of the multi-shell FWVF with age that had not been described

previously, the existence of a posterior-anterior gradient and the region-specific nature of the changes of the water fraction across the adult lifespan. Additionally, the multi-shell FWVF showed a linear correlation with volumetric parameters such as the brain volume, cerebral WM volume and ventricles volume (Fig. 4d-f). Finally, we confirmed that the DTI scalar measures do modify with age, following a U-shaped trajectory as previously observed by other authors (Westlye et al., 2010; Lebel et al., 2012; Beck et al., 2021). However, in this work, we have detected that those trajectories were deeply influenced by the FW component. Once the FWVF is removed, scalar measures demonstrate a significantly reduced variability over the adult lifespan compared to those calculated from standard DTI (Fig. 5b,c, Supplementary Fig. 6, Supplementary Fig. 7).

The first contribution, then, is to uncover the non-linear behavior and the heteroskedastic nature of the variation of the multi-shell derived FWVF with age. As indicated above, this variation of the FWVF with age was already known and it had been previously studied by other authors. However, those studies differ from ours in three main aspects: (1) the methodology used to estimate the FWVF, (2) the regions considered for the study; and (3) the way in which the behavior is modeled. First, our study employs the spherical means-based technique with multiple-shell acquisitions that represents diffusion using a continuous mixture of axis-symmetric second-order tensors in the space of orientations. This procedure enables us to estimate the FWVF more accurately than optimizing the bi-tensor signal representation, especially under a crossing fibers scenario (see page 27 in Supplementary materials and Supplementary Fig. 8). Regarding the second aspect, some studies are limited to the WM skeleton or to specific regions (Metzler-Baddeley et al., 2012; Chad et al., 2018), while our study covers the whole WM in a region-specific manner. Regarding the modeling, our study employs a polynomial approach with a QR optimization to represent the variations in the FWVF as a function of age. This allows us to consider that the variability of the parameters being investigated across the lifespan may be associated with age, i.e., follow a heteroskedastic pattern. To our best knowledge, the heteroskedastic modeling of the dMRI parameters has not been properly handled in the literature before.

Some previous endeavors considered a linear approach with homoskedastic assumptions on the FWVF and/or are limited to a selected period of life (Metzler-Baddeley et al., 2012; Chad et al., 2018). Additionally, even when a non-linear model is used to represent the trajectory of FWVF (Kubicki et al., 2019), it is optimized *via* the non-linear least squares approach where no heteroskedastic assumptions are possible on the dependent variable. Despite the fact that this polynomial model is well-accepted in the community to account for the variations in diffusion parameters of the brain (Westlye et al., 2010; Beck et al., 2021; Kiely et al., 2022), some studies suggest more *avant-garde* models such as a Poisson curve to account for different changing rates in childhood and aging life stages (Lebel et al., 2012; Kubicki et al., 2019). Nonetheless, compared to our study, these reports used a quadratic cost function in a non-linear fitting procedure and do not allow for modeling the heteroskedastic nature of the parameter, which implicitly assume that the variability of the residual term of the parameter being investigated across the lifespan is not associated with age. Our study provides
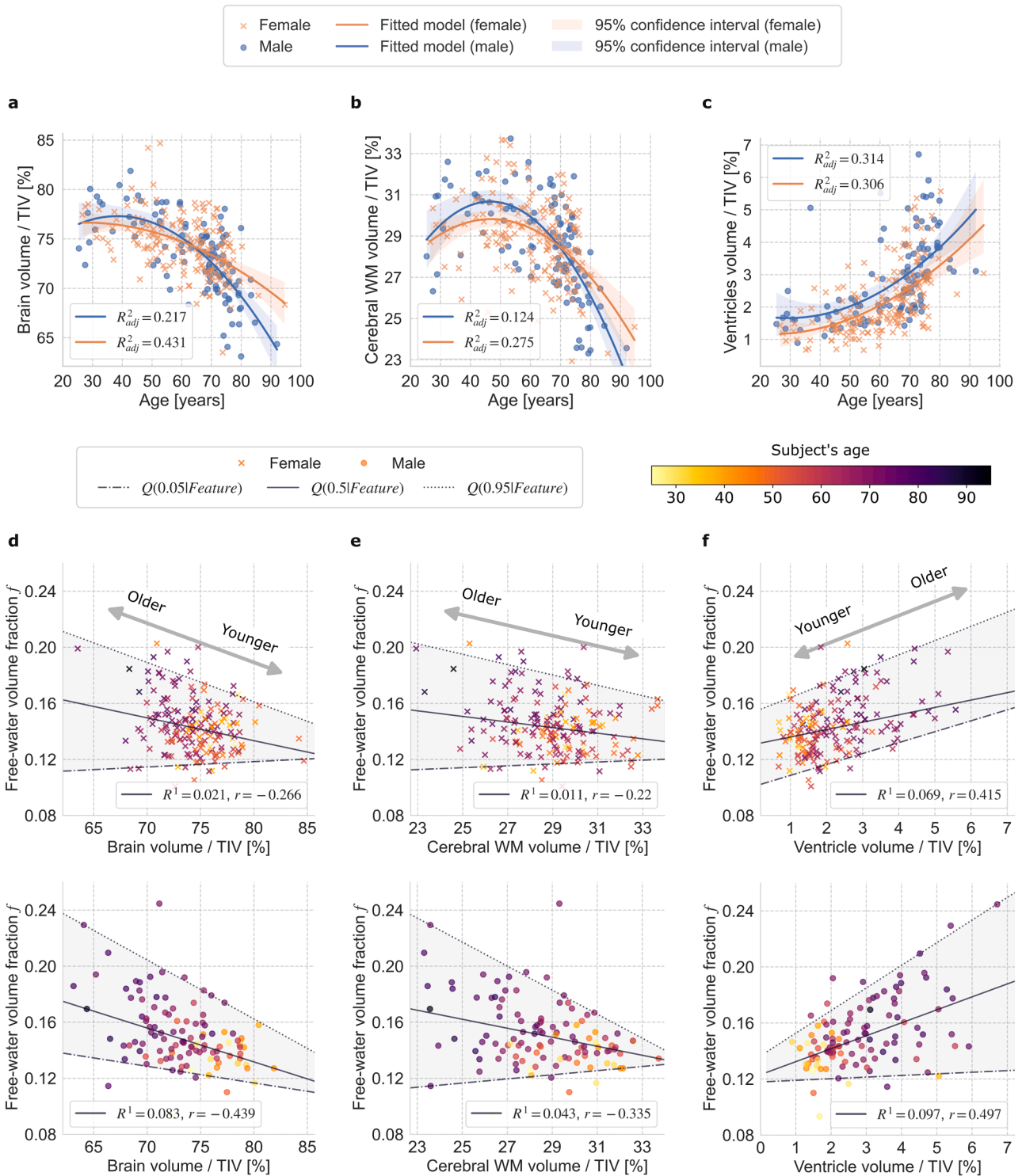
Figure 4. a-c: Adult lifespan variations in volumetry-based features of the brain as a function of age (given in years) are presented separately for male and female subjects: a brain volume, b a cerebral WM volume and c ventricles volume. All volume-based features are given in normalized units by the total intracranial volumes (TIV, given in %). The second-order polynomial models were fitted separately for female and male subjects using a linear regression. The adjusted R-squared R_{adj}^2 parameter characterizes all fitted models. The shaded regions show the 95% confidence intervals estimated from 10,000 bootstrap resamples. d-e: The FWVF f as a function of volume-based features (*Feature* ∈ {*Brain volume, Cerebral WM volume, Ventricles volume*}) normalized by the TIV, presented separately for female (top row) and male subjects. An individual marker delivers a median value of the FWVF f computed from the WM in the native space of a single subject. The linear QR (see Eq. (7) in Methods) is used to model the relationship between the FWVF f and the volume-based features of the brain: d brain volume, e cerebral WM volume and f ventricles volume. The color of the marker refers to the age of the subject and follows the colorbar included in the right top. The solid lines represent the function $Q(0.5|Feature)$, the dashed-dotted lines show $Q(0.05|Feature)$ and the dotted lines represent $Q(0.95|Feature)$. The regions between $Q(0.05|Age)$ and $Q(0.95|Age)$ were shaded for visualization purposes. The goodness-of-fit R^1 at $\tau = 0.5$ and Pearson's correlation coefficient r are provided separately for each plot. The arrows show the directions presenting changes in subjects' age. The experiments employ only cross-sectional samples.
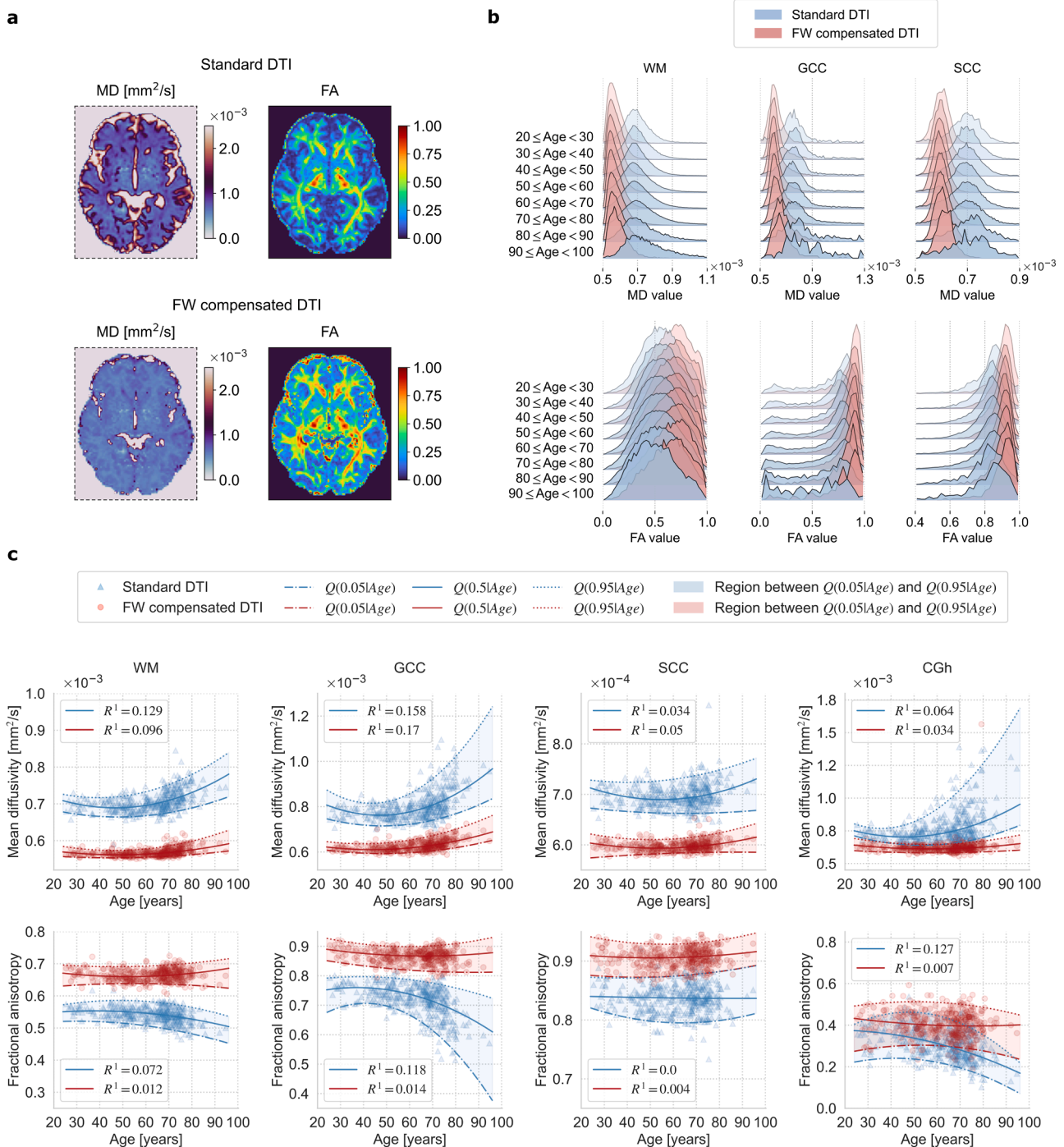
Figure 5. a Visual inspection of DTI-based measures based on a standard single-component DTI representation with no FWVF assumption (i.e., $f = 0$) and with a FW compensated DTI. The MD/FA measures were calculated for a randomly chosen healthy male subject at the age of 69 and are shown in a selected axial plane. b The density plots presenting the sample variations in MD [mm^2/s] and FA estimated under the standard DTI and FW compensated DTI over the age intervals defined in Table 1. The experiment reports the qualitative MD and FA variations using only cross-sectional samples. The number of bins for each density plot were determined separately for each age interval using the formula built upon Doane's method. The population-based experiment uses only cross-sectional samples. c Estimated MD/FA measures using a standard DTI and with a FW compensation, and their trajectories across the adult lifespan modeled *via* the QR technique using Model 1 (see Eq. (4) in Methods). The experiment uses cross-sectional and longitudinal samples. Each marker represents the median value of the measure calculated over the ROI in the subject's native space. The solid lines show the quantile function $Q(0.5|Age)$, the lower dashed-dotted lines indicate $Q(0.05|Age)$, and the upper dotted lines present $Q(0.95|Age)$, all three were computed for a standard DTI (blue lines) and FW compensated DTI (red lines). The regions between $Q(0.05|Age)$ and $Q(0.95|Age)$ were shaded for visualization purposes. The goodness-of-fit R^1 at $\tau = 0.5$ was computed separately for a standard DTI and FW compensated DTI measures using the procedure introduced by Koenker and Machado (1999).

evidence to suggest that this is not the case. The polynomial approach enables us to handle this phenomenon and to model different quantiles, providing a measure of uncertainty of the parameters. Moreover, the linear QR, contrary to the non-linear models, enabled us to evaluate the significances of the corresponding age-related terms. The current study goes much further and enables us to handle both cross-sectional and longitudinal data. The preceding studies in dMRI parameters alterations with age merely juxtaposed young and older subjects (Burzynska et al., 2010; Bennett et al., 2010), evaluated the cross-sectional data (Westlye et al., 2010; Lebel et al., 2012; Metzler-Baddeley et al., 2012; Cox et al., 2016; Chad et al., 2018; Kiely et al., 2022) or longitudinal measurements (Ofori et al., 2015), with rudimentary studies considering both (Maillard et al., 2019; Beck et al., 2021).

Another major contribution of this work is to unveil how the single-shell DTI related metrics are affected by the FWVF retrieved from multi-shell acquisitions with age. This part of the study gathers two previously known effects that have been studied separately: (1) the change of diffusion metrics with age: when single-component DTI is considered, diffusion measures in the healthy WM of the human brain present a curvilinear U-form across the lifespan. FA shows a growth in early adulthood and then a systematic decline, while MD reveals the opposite trend (Westlye et al., 2010; Lebel et al., 2012; Beck et al., 2021); (2) the effect of the FWVF on DTI-based measures, which has been studied previously for single-shell acquisitions (Pasternak et al., 2009; Metzler-Baddeley et al., 2012; Chad et al., 2018; Kubicki et al., 2019), with some preliminary research on differences with age (Metzler-Baddeley et al., 2012; Chad et al., 2018; Kubicki et al., 2019), and under the impact of neurodegenerative diseases (Bergamino et al., 2021; Carreira Figueiredo et al., 2022).

In this work, in order to study the two effects jointly, we examined the variability in the MD and FA across the adult lifespan under two different scenarios: standard DTI and the FW compensated DTI. Our results show that the FW component significantly affects the DTI measures with age. When standard DTI is considered, FA and MD shows the U-form behavior across the lifespan, compatible with findings in Westlye et al. (2010), Lebel et al. (2012), and Beck et al. (2021). On the other hand, when the two-component representation given by Eq. (3) is assumed, and the influence of the FW is reduced, we observe a flattening effect of the MD and FA measures or the trend reversal for the FA compared to the standard DTI (see Fig. 5b,c, Supplementary Fig. 6, Supplementary Fig. 7). The flattening effect of the MD parameter has previously been noticed in the fornix with adult subjects (Metzler-Baddeley et al., 2012) and suggested in MD and FA measures over the WM skeleton through a significant decrease in the absolute correlation coefficient with age (Chad et al., 2018). This study has not confirmed the FW corrected FA behavior over the brain WM what others had found in the fornix area (Metzler-Baddeley et al., 2012), i.e., further negative increase in the elevation of the parameter with age. Instead, we observe reduced dynamics of the FA measure under a FW compensation (compatible with Chad et al. (2018)), reflected in a decrease in R^1 parameter or the enhancement of a convex trajectory of the FA, reflected in an increased R^1 and an increased quadratic coefficient of the model. Interestingly, the opposite behavior of the FA measure is observed after the correction, i.e., concave trajectories switch to convex. The variability reduction in DTI-based measures under the FW compensation has been previously observed by Albi et al. (2017) and explained as an increase in reproducibility. However, our results explain that the FW correction reduces the variability of the MD/FA measures across lifespan but does not necessarily imply an improvement in their reproducibility.

Different authors have studied the variation of the FA across the lifespan without considering the FWVF and, therefore, they have tried to explain this effect differently. Vernooij et al. (2008) explained the age-related decrease in FA by atrophy and lesion formation. This hypothesis was rejected by Westlye et al. (2010), where authors pointed out that such pathological factors cannot have a significant impact on

healthy young subjects. Alternatively, they hypothesized that the formation of redundant myelin and water compartments may increase volume and decrease FA with age. Bennett et al. (2010), Burzynska et al. (2010) and Lebel et al. (2012) also relate FA alterations with changes of myelination and/or axonal density.

All in all, our results indicate that the changes in the FW component constitute a major factor to explain the variability of DTI metrics with age. This issue must be taken into account when using these metrics for clinical studies. Depending on the ages of the participants, data can present some bias due to the lifespan related alterations. Fortunately, if the dMRI acquisition comprises at least two different shells, the estimation of the FWVF is feasible and it is possible to correct the age-related bias. In addition, when comparing scalar measures like FA and MD in healthy and pathological subjects, it is tempting to explain the differences between groups as the result of underlying biological effects: the reduction of myelin, modifications of the axonal density. In the light of our experiments, we should be more cautious in explaining microstructural processes from the results obtained from diffusion measures, since there may be unconsidered factors at play, such as the FWVF.

This study presents several limitations that must be noted. First, a relatively small sample size was employed ($N = 287$), and the distribution of the samples across the age intervals was non-uniform. However, compared to the previous studies modeling the free-water fraction variations across the lifespan (Metzler-Baddeley et al., 2012; Cox et al., 2016; Chad et al., 2018), our population sample has been spread over the whole adult life, including subjects from early adulthood until senescence. Moreover, the sample includes a mixed cross-sectional and longitudinal design that enables us to model the FWVF over the lifespan, including changes over time, suppressing the effect of inter-subject variability. In the present study, however, we modeled the longitudinal observations as independent under the QR framework. Although one can employ a more suitable method to delineate the FWVF behavior across the adult lifespan from cross-sectional and longitudinal data together, such as the Linear Quantile Mixed Models (Geraci and Bottai, 2014), we did not observe significant deviations from the results obtained with the QR approach (results not shown).

Secondly, as with most image-based population studies, the current study is limited by the registration procedure. The approach used in our study follows the well-accepted standard community pipeline, i.e., we non-linearly register the FA to the FSL template "FMRIB58_FA" and then inversely warp the atlas ROIs to the subjects' native spaces using the FSL software suite. A proper registration procedure and template selection are critical for ROI-based studies as the misalignment might bias the representative values. Recently, Wu et al., (2022) proposed a new FA template that meets the requirements of lifespan studies and reduces possible misalignment artifacts in elderly brains. Here, however, each ROI had been morphologically eroded before all analyses took place to exclude potential outliers exposed to the partial volume effect. In fact, the ROI-based analysis might be considered a deficiency as such. Nonetheless, some previous lifespan studies in diffusion MRI (Kiely et al., 2022) follow this line since it is standardized, as mentioned above.

Additionally, we limited the scope of the water component to the simplest form of diffusion representation, DTI, although one can extrapolate the study and incorporate more advanced dMRI signal representations such as diffusion kurtosis imaging (DKI) (Jensen et al., 2005) or the propagator-based metrics (Özarslan et al., 2013; Tristán-Vega and Aja-Fernández, 2021). For instance, the DKI includes information beyond the standard DTI appearing at a higher b-value regime (Jensen et al., 2005), while the propagator-based measures can catch the axial or planar diffusion profiles (Özarslan et al., 2013). The proper water-correction of these dMRI signal representations might lead us to new insights into modeling the non-Gaussian diffusion profiles and unbiased indicators of restrictive diffusion and cellularity across the lifespan.

Finally, another limitation of the study is related to the method made use of to estimate the FWVF. The spherical means approach depicts the

cellular compartment with a single component compared to biophysical models such as the neurite orientation dispersion and density imaging (NODDI; Zhang et al., 2012). This reduction in the complexity of a cellular compartment might translate to the FWVF parameter bias. However, as illustrated in Supplementary Fig. 8, this potential bias in the FWVF is considered to be negligible. The spherical means method adapts the general formulation from Tristán-Vega and Aja-Fernández (2021) by fixing the parallel diffusivity in Eq. (2) over the white matter area to $\lambda_{par} = 2.1 \cdot 10^{-3}$ mm^2/s. This way, the FWVF can be estimated from just two different acquired shells. However, as recently shown by Tristán-Vega and Aja-Fernández (2021), the parameter λ_{par} can be constant over the WM tissue without the repercussions of further inferences. Guerrero et al. (2019) has additionally shown that the parallel diffusivity used in the NODDI does not vary appreciably with age over the WM unless the population group includes infants or adolescent subjects and has no sex effects. Although our quantitative studies focus exclusively on the WM area, the fixed parallel diffusivity λ_{par} should be refined once studying the GM, as recently noticed by Guerrero et al. (2019) for the NODDI, or estimated from the data along with the FWVF using the spherical means approach given a three or more shell acquisition protocol. As illustrated in Supplementary Fig. 8, the spherical means technique achieves a smaller estimation error from two-shell data than the bi-tensor approach (Hoy et al., 2014; Bergmann et al., 2020) and the NODDI through the accelerated microstructure imaging *via* convex optimization (AMICO; Daducci et al., 2015). The spherical means approach is also relatively robust to selecting a particular value of the regularization parameter ν (see Supplementary Fig. 9). However, inaccurately choosing the parallel diffusivity λ_{par} may lead to biases in estimating the FWVF. These biases are comparable to those introduced by the NODDI via the AMICO and far more modest than those calculated with the bi-tensor representation. Last, a fixed value of parallel diffusivity λ_{par} in the spherical means technique might also somewhat explain the observed growths of the FWVF parameter and flatted age-related changes in the FW corrected DTI metrics.

Finally, we notice, as the FW and hindered water follow different signal decays, that they can be separated using dedicated MRI machines equipped with high-strength gradients (Afzali et al., 2022). However, using ultra-strong gradients (up to 300 mT/m) exceeds the current technical capabilities in versatile population studies, imposing a clinical scanner with a common gradient strength, as about 40 mT/m employed in this study.

6. Conclusions

This paper studies the evolution of the spherical means-based FWVF estimated from multi-shell diffusion MRI in the healthy human brain WM across the adult lifespan. It also gains insight into the effects of the compensation of DTI measures for FW in these analyses. Much of existing clinical research involves juxtaposing the population groups to find the differences occurring in the brain due to an illness or under a specific condition. However, modern and successful brain research requires more than standard group-based comparisons and new directions related to trajectory-based tracking of diseases are expected to gain interest in the near future. This raises new challenges in the neuroimaging field, with a particular emphasis on capturing the onset of neurodegenerative disease and predicting further alterations of the brain.

Ethical statement

The study was conducted in line with the Declaration of Helsinki and has been reviewed and approved by the Regional Committee for Medical and Health Research Ethics (REC), South East division in Norway (2014/694, 2009/2485).

Code availability

The FWVF was estimated with the dMRI-Lab toolbox (https://www.lpi.tel.uva.es/dmrilab) implemented in MATLAB (The MathWorks, Inc., Natick, MA).

CRediT authorship contribution statement

Tomasz Pieciak: Conceptualization, Methodology, Software, Validation, Formal analysis, Investigation, Data curation, Writing – original draft, Writing – review & editing, Visualization, Project administration. **Guillem París:** Software, Writing – review & editing. **Dani Beck:** Resources, Data curation, Writing – review & editing. **Ivan I. Maximov:** Resources, Data curation, Writing – review & editing. **Antonio Tristán-Vega:** Conceptualization, Methodology, Software, Validation, Writing – review & editing, Visualization, Supervision. **Rodrigo de Luis-García:** Methodology, Validation, Writing – review & editing. **Lars T. Westlye:** Writing – review & editing, Supervision, Funding acquisition. **Santiago Aja-Fernández:** Conceptualization, Validation, Writing – original draft, Writing – review & editing, Supervision, Project administration, Funding acquisition.

Declaration of Competing Interest

The authors declare that they have no known competing financial interests or personal relationships that could have appeared to influence the work reported in this paper.

Data availability

Data will be made available on request.

Acknowledgements

Supplementary materials

Supplementary material associated with this article can be found, in the online version, at doi:10.1016/j.neuroimage.2023.120324.

References

Afzali, M., Pieciak, T., Jones, D.K., Schneider, J.E., Ozarslan, E., 2022. Cumulant Expansion with Localization: A new representation of the diffusion MRI signal. Frontiers in Neuroimaging 1. https://doi.org/10.3389/fnimg.2022.958680.

Akaike, H., 1974. A new look at the statistical model identification. IEEE transactions on automatic control 19 (6), 716–723.

Allen, J.S., Damasio, H., Grabowski, T.J., 2002. Normal neuroanatomical variation in the human brain: an MRI-volumetric study. American Journal of Physical Anthropology 118 (4), 341–358.

Albi, A., et al., 2017. Free water elimination improves test–retest reproducibility of diffusion tensor imaging indices in the brain: A longitudinal multisite study of healthy elderly subjects. Human Brain Mapping 38 (1), 12–26.

Andersson, J.L.R., Skare, S., Ashburner, J., 2003. How to correct susceptibility distortions in spin-echo echo-planar images: application to diffusion tensor imaging. NeuroImage 20 (2), 870–888.

Assaf, Y., Freidlin, R.Z., Rohde, G.K., Basser, P.J., 2004. New modeling and experimental framework to characterize hindered and restricted water diffusion in brain white matter. Magnetic Resonance in Medicine 52 (5), 965–978.

Basser, P.J., Mattiello, J., LeBihan, D., 1994. MR diffusion tensor spectroscopy and imaging. Biophysical journal 66 (1), 259–267.

Beck, D., et al., 2021. White matter microstructure across the adult lifespan: A mixed longitudinal and cross-sectional study using advanced diffusion models and brain-age prediction. NeuroImage 224, 117441.

Bethlehem, R.A., et al., 2022. Brain charts for the human lifespan. Nature 604 (7906), 525–533.

Bennett, I.J., Madden, D.J., Vaidya, C.J., Howard, D.V., Howard-Jr, J.H., 2010. Age-related differences in multiple measures of white matter integrity: A diffusion tensor imaging study of healthy aging. Human brain mapping 31 (3), 378–390.

Bergamino, M., Pasternak, O., Farmer, M., Shenton, M.E., Hamilton, J.P., 2016. Applying a free-water correction to diffusion imaging data uncovers stress-related neural pathology in depression. NeuroImage: Clinical 10, 336–342.

Bergamino, M., Walsh, R.R., Stokes, A.M., 2021. Free-water diffusion tensor imaging improves the accuracy and sensitivity of white matter analysis in Alzheimer's disease. Scientific reports 11 (1), 1–12.

Berger, M., et al., 2022. Free water diffusion MRI and executive function with a speed component in healthy aging. NeuroImage, 119303.

Bergmann, Ø., Henriques, R., Westin, C.F., Pasternak, O., 2020. Fast and accurate initialization of the free-water imaging model parameters from multi-shell diffusion MRI. NMR in Biomedicine 33 (3), e4219.

Billiet, T., et al., 2015. Age-related microstructural differences quantified using myelin water imaging and advanced diffusion MRI. Neurobiology of aging 36 (6), 2107–2121.

Brent, R.P., 1973. Some efficient algorithms for solving systems of nonlinear equations. SIAM Journal on Numerical Analysis 10 (2), 327–344.

Breusch, T.S., Pagan, A.R., 1979. A simple test for heteroscedasticity and random coefficient variation. Econometrica: Journal of the econometric society 1287–1294.

Burzynska, A.Z., et al., 2010. Age-related differences in white matter microstructure: region-specific patterns of diffusivity. Neuroimage 49 (3), 2104–2112.

Carreira Figueiredo, I., Borgan, F., Pasternak, O., Turkheimer, F.E., Howes, O.D., 2022. White-matter free-water diffusion MRI in schizophrenia: a systematic review and meta-analysis. Neuropsychopharmacology 47 (7), 1413–1420.

Cetin-Karayumak, S., et al., 2020. White matter abnormalities across the lifespan of schizophrenia: a harmonized multi-site diffusion MRI study. Molecular psychiatry 25 (12), 3208–3219.

Chad, J.A., Pasternak, O., Salat, D.H., Chen, J.J., 2018. Re-examining age-related differences in white matter microstructure with free-water corrected diffusion tensor imaging. Neurobiology of aging 71, 161–170.

Chang, Y.S., et al., 2015. White matter changes of neurite density and fiber orientation dispersion during human brain maturation. PloS one 10 (6), e0123656.

Chung, A.W., Seunarine, K.K., Clark, C.A., 2016. NODDI reproducibility and variability with magnetic field strength: a comparison between 1.5 T and 3 T. Human brain mapping 37 (12), 4550–4565.

Cox, S.R., et al., 2016. Ageing and brain white matter structure in 3,513 UK Biobank participants. Nature communications 7 (1), 1–13.

Daducci, A., Canales-Rodríguez, E.J., Zhang, H., Dyrby, T.B., Alexander, D.C., Thiran, J. P., 2015. Accelerated microstructure imaging via convex optimization (AMICO) from diffusion MRI data. Neuroimage 105, 32–44.

Dekaban, A.S., Sadowsky, D., 1978. Changes in brain weights during the span of human life: relation of brain weights to body heights and body weights. Annals of Neurology 4 (4), 345–356.

Doane, D.P., 1976. Aesthetic frequency classifications. The American Statistician 30 (4), 181–183.

Edde, M., et al., 2020. Free water: A marker of age-related modifications of the cingulum white matter and its association with cognitive decline. PloS one 15 (11), e0242696.

Ellis, R.S., 1920. Norms for some structural changes in the human cerebellum from birth to old age. Journal of Comparative Neurology 32 (1), 1–33.

Fischl, B., et al., 2002. Whole brain segmentation: automated labeling of neuroanatomical structures in the human brain. Neuron 33 (3), 341–355.

Geraci, M., Bottai, M., 2014. Linear quantile mixed models. Statistics and computing 24, 461–479.

Gogtay, N., et al., 2004. Dynamic mapping of human cortical development during childhood through early adulthood. Proceedings of the National Academy of Sciences 101 (21), 8174–8179.

Golub, M., Neto-Henriques, R., Gouveia-Nunes, R., 2021. Free-water DTI estimates from single b-value data might seem plausible but must be interpreted with care. Magnetic resonance in medicine 85 (5), 2537–2551.

Guerrero, J.M., et al., 2019. Optimizing the intrinsic parallel diffusivity in NODDI: an extensive empirical evaluation. PloS one 14 (9), e0217118.

Head, D., et al., 2004. Differential vulnerability of anterior white matter in nondemented aging with minimal acceleration in dementia of the Alzheimer type: evidence from diffusion tensor imaging. Cerebral cortex 14 (4), 410–423.

Hill, R.A., Li, A.M., Grutzendler, J., 2018. Lifelong cortical myelin plasticity and age-related degeneration in the live mammalian brain. Nature neuroscience 21 (5), 683–695.

Hoy, A.R., Koay, C.G., Kecskemeti, S.R., Alexander, A.L., 2014. Optimization of a free water elimination two-compartment model for diffusion tensor imaging. Neuroimage 103, 323–333.

Jensen, J.H., Helpern, J.A., Ramani, A., Lu, H., Kaczynski, K., 2005. Diffusional kurtosis imaging: the quantification of non-gaussian water diffusion by means of magnetic resonance imaging. Magnetic Resonance in Medicine 53 (6), 1432–1440.

Jeurissen, B., Leemans, A., Tournier, J.D., Jones, D.K., Sijbers, J., 2013. Investigating the prevalence of complex fiber configurations in white matter tissue with diffusion magnetic resonance imaging. Human brain mapping 34 (11), 2747–2766.

Kaden, E., Kelm, N.D., Carson, R.P., Does, M.D., Alexander, D.C., 2016. Multi-compartment microscopic diffusion imaging. NeuroImage 139, 346–359.

Keijzer, H., et al., 2023. Free water corrected diffusion tensor imaging discriminates between good and poor outcomes of comatose patients after cardiac arrest. European radiology 33 (3), 2139–2148.

Kellner, E., Dhital, B., Kiselev, V.G., Reisert, M., 2016. Gibbs-ringing artifact removal based on local subvoxel shifts. Magnetic resonance in medicine 76 (5), 1574–1581.

Kemper, T., Albert, M.L., Knoefel, J., 1994. Neuroanatomical and neuropathological changes during aging and dementia. Clinical Neurology of Aging. Oxford University Press, New York, pp. 3–67.

Kiely, M., et al., 2022. Insights into human cerebral white matter maturation and degeneration across the adult lifespan. NeuroImage 247, 118727.

Kodiweera, C., Alexander, A.L., Harezlak, J., McAllister, T.W., Wu, Y.C., 2016. Age effects and sex differences in human brain white matter of young to middle-aged adults: A DTI, NODDI, and q-space study. Neuroimage 128, 180–192.

Koenker, R., 1981. A note on studentizing a test for heteroscedasticity. Journal of econometrics 17 (1), 107–112.

Koenker, R., Machado, J.A., 1999. Goodness of fit and related inference processes for quantile regression. Journal of the american statistical association 94 (448), 1296–1310.

Koenker, R., Hallock, K.F., 2001. Quantile regression. Journal of economic perspectives 15 (4), 143–156.

Kubicki, M., et al., 2007. A review of diffusion tensor imaging studies in schizophrenia. Journal of psychiatric research 41 (1-2), 15–30.

Kubicki, M., et al., 2019. Lifespan trajectories of white matter changes in rhesus monkeys. Cerebral Cortex 29 (4), 1584–1593.

Lebel, C., et al., 2012. Diffusion tensor imaging of white matter tract evolution over the lifespan. Neuroimage 60 (1), 340–352.

Lucignani, M., et al., 2021. Reliability on multiband diffusion NODDI models: a test retest study on children and adults. Neuroimage 238, 118234.

Lyall, A.E., et al., 2018. Greater extracellular free-water in first-episode psychosis predicts better neurocognitive functioning. Molecular psychiatry 23 (3), 701–707.

MacDonald, M.E., Pike, G.B., 2021. MRI of healthy brain aging: A review. NMR in Biomedicine 34 (9), e4564.

Maillard, P., et al., 2019. Cerebral white matter free water: A sensitive biomarker of cognition and function. Neurology 92 (19), e2221–e2231.

Maximov, I.I., Alnæs, D., Westlye, L.T., 2019. Towards an optimised processing pipeline for diffusion magnetic resonance imaging data: Effects of artefact corrections on diffusion metrics and their age associations in UK Biobank. Human Brain Mapping 40 (14), 4146–4162.

Merluzzi, A.P., et al., 2016. Age-dependent differences in brain tissue microstructure assessed with neurite orientation dispersion and density imaging. Neurobiology of aging 43, 79–88.

Metz, M.C., et al., 2020. Predicting glioblastoma recurrence from preoperative MR scans using fractional-anisotropy maps with free-water suppression. Cancers 12 (3), 728.

Metzler-Baddeley, C., O'Sullivan, M.J., Bells, S., Pasternak, O., Jones, D.K., 2012. How and how not to correct for CSF-contamination in diffusion MRI. Neuroimage 59 (2), 1394–1403.

Mori, S., Wakana, S., Van Zijl, P.C., Nagae-Poetscher, L.M., 2005. MRI atlas of human white matter. Elsevier.

Nave, K.A., 2010. Myelination and support of axonal integrity by glia. Nature 468 (7321), 244–252.

Nairn, J.G., Bedi, K.S., Mayhew, T.M., Campbell, L.F., 1989. On the number of Purkinje cells in the human cerebellum: unbiased estimates obtained by using the "fractionator. Journal of Comparative Neurology 90, 527–532.

Ofori, E., et al., 2015. Longitudinal changes in free-water within the substantia nigra of Parkinson's disease. Brain 138 (8), 2322–2331.

Özarslan, E., 2013. Mean apparent propagator (MAP) MRI: a novel diffusion imaging method for mapping tissue microstructure. NeuroImage 78, 16–32.

Pakkenberg, B., Gundersen, H.J., 1997. Neocortical neuron number in humans: effect of sex and age. Journal of Comparative Neurology 384, 312–320.

Pasternak, O., Sochen, N., Gur, Y., Intrator, N., Assaf, Y., 2009. Free water elimination and mapping from diffusion MRI. Magnetic Resonance in Medicine 62 (3), 717–730.

Pasternak, O., Shenton, M.E., Westin, C.F., 2012. Estimation of extracellular volume from regularized multi-shell diffusion MRI. In: International Conference on Medical Image Computing and Computer-Assisted Intervention. Springer, pp. 305–312.

Pasternak, O., Kubicki, M., Shenton, M.E., 2016. In vivo imaging of neuroinflammation in schizophrenia. Schizophrenia research 173 (3), 200–212.

Pierpaoli, C., Jones, D. K. Removing CSF contamination in brain DT-MRIs by using a two-compartment tensor model. In International Society for Magnetic Resonance in Medicine Meeting (p. 1215) (2004).

Peters, A., 2002. The effects of normal aging on myelin and nerve fibers: a review. Journal of neurocytology 31 (8), 581–593.

Planche, V., et al., 2022. Structural progression of Alzheimer's disease over decades: the MRI staging scheme. Brain Communications 4 (3), fcac109.

Ray, N.J., et al., 2023. Free-water imaging of the cholinergic basal forebrain and pedunculopontine nucleus in Parkinson's disease. Brain 146 (3), 1053–1064.

Raghavan, S., et al., 2021. Diffusion models reveal white matter microstructural changes with ageing, pathology and cognition. Brain communications 3 (2), fcab106.

Roalf, D.R., et al., 2016. The impact of quality assurance assessment on diffusion tensor imaging outcomes in a large-scale population-based cohort. Neuroimage 125, 903–919.

Rutherford, S., et al., 2022. Charting brain growth and aging at high spatial precision. Elife 11, e72904.

Rydhög, A.S., et al., 2017. Separating blood and water: Perfusion and free water elimination from diffusion MRI in the human brain. Neuroimage 156, 423–434.

Skullerud, K., 1985. Variations in the size of the human brain, Influence of age, sex, body length, body mass index, alcoholism, Alzheimer changes, and cerebral atherosclerosis. Acta Neurol Scand Suppl 102, 1–94.

Sowell, E.R., et al., 2003. Mapping cortical change across the human life span. Nature neuroscience 6 (3), 309–315.

Sowell, E.R., et al., 2007. Sex differences in cortical thickness mapped in 176 healthy individuals between 7 and 87 years of age. Cerebral cortex 17 (7), 1550–1560.

Smith, S.M., et al., 2004. Advances in functional and structural MR image analysis and implementation as FSL. NeuroImage 23 (S1), 208–219.

Šimić, G., Kostović, I., Winblad, B., Bogdanović, N., 1997. Volume and number of neurons of the human hippocampal formation in normal aging and Alzheimer's disease. Journal of Comparative Neurology 379 (4), 482–494.

Tristán-Vega, A., Aja-Fernández, S., 2021. Efficient and accurate EAP imaging from multi-shell dMRI with micro-structure adaptive convolution kernels and dual Fourier Integral Transforms (MiSFIT). NeuroImage 227, 117616.

Tristán-Vega, A., París, G., de Luis-García, R., Aja-Fernández, S., 2022. Accurate free-water estimation in white matter from fast diffusion MRI acquisitions using the spherical means technique. Magnetic Resonance in Medicine 87 (2), 1028–1035.

Veraart, J., et al., 2016. Denoising of diffusion MRI using random matrix theory. Neuroimage 142, 394–406.

Vernooij, M., et al., 2008. White matter atrophy and lesion formation explain the loss of structural integrity of white matter in aging. Neuroimage 43 (3), 470–477.

Westin, C.F., et al., 2002. Processing and visualization for diffusion tensor MRI. Medical image analysis 6 (2), 93–108.

Westlye, L.T., et al., 2010. Life-span changes of the human brain white matter: diffusion tensor imaging (DTI) and volumetry. Cerebral cortex 20 (9), 2055–2068.

Wu, Y., et al., 2022. Development of high quality T1-weighted and diffusion tensor templates of the older adult brain in a common space. NeuroImage 260, 119417.

Zhang, H., Schneider, T., Wheeler-Kingshott, C.A., Alexander, D.C., 2012. NODDI: practical in vivo neurite orientation dispersion and density imaging of the human brain. Neuroimage 61 (4), 1000–1016.